

A Trainable Centrality Framework for Modern Data

Minh Duc Vu*

MINHDUC.VU@U.NUS.EDU

*Department of Statistics and Data Science
National University of Singapore*

Mingshuo Liu*

MSHLIU@UCDAVIS.EDU

*Department of Statistics
University of California, Davis*

Doudou Zhou†

DDZHOU@NUS.EDU.SG

*Department of Statistics and Data Science
National University of Singapore*

Abstract

Measuring how central or typical a data point is underpins robust estimation, ranking, and outlier detection, but classical depth notions become expensive and unstable in high dimensions and are hard to extend beyond Euclidean data. We introduce Fused Unified centrality Score Estimation (FUSE), a neural centrality framework that operates on top of arbitrary representations. FUSE combines a global head, trained from pairwise distance-based comparisons to learn an anchor-free centrality score, with a local head, trained by denoising score matching to approximate a smoothed log-density potential. A single parameter between 0 and 1 interpolates between these calibrated signals, yielding depth-like centrality from different views via one forward pass. Across synthetic distributions, real images, time series, and text data, and standard outlier detection benchmarks, FUSE recovers meaningful classical ordering, reveals multi-scale geometric structures, and attains competitive performance with strong classical baselines while remaining simple and efficient.

Keywords: Centrality measure, High-dimensional/Non-Euclidean data, Neural networks, Score-based models

1 Introduction

Quantifying how central or peripheral a data point is relative to a distribution is a core tool in statistics and machine learning. A single centrality score provides a unified way to describe data. It supports robust estimation such as depth-based medians and trimming (Tukey, 1975), induces multivariate rankings for visualization and summarization (Liu, 1990), and underlies classical approaches to outlier detection and robust inference (Donoho and Gasko, 1992). Foundational notions include the spatial (L_1) depth and multivariate median (Vardi and Zhang, 2000), spatial quantile depth (Serfling, 2002), and projection depth (Zuo, 2003). Other important centrality measures include Mahalanobis depth (Mahalanobis, 1936), kernel density centrality (Parzen, 1962), and potential depth (Pokotylo

*. Vu and Liu contributed equally to this work.

†. Corresponding author.

and Mosler, 2019). These works have established data depth as a central concept for robust, interpretable multivariate analysis.

Building on these foundations, recent work has extended depth to more general data types. Examples include depths for functional data that handle partially observed trajectories (Elías et al., 2023), depths for non-Euclidean or object-valued data (Dai et al., 2023), and unified depths for mixed or complex data (Blocher and Schollmeyer, 2024). Such extensions broaden the reach of depth, but also reveal that many computational and inferential challenges persist in modern applications.

Despite their appeal, classical depth notions face several key limitations in modern settings. First, many classical depths become impractical computationally or statistically as the sample size n and dimension d grow. Exact halfspace (Tukey) and projection depths become infeasible beyond moderate d (Dyckerhoff and Mozharovskiy, 2016; Dyckerhoff et al., 2021; Fojtík et al., 2024), while Mahalanobis depth depends on accurate covariance estimation, which is unreliable when d is comparable to or larger than n . Second, in high dimensions, pairwise distances concentrate and hubs emerge (Beyer et al., 1999; Radovanovic et al., 2010; Feldbauer and Flexer, 2019), and the data often lie near a low-dimensional manifold (Belkin et al., 2006; Fefferman et al., 2016; Meilă and Zhang, 2024), weakening the meaning of distance-based centrality in raw feature space. Third, most classical definitions capture primarily global centrality, describing how a point relates to the overall cloud, while providing limited resolution for local centrality, i.e., how typical a point is within its neighborhood. For example, points near the center of a cluster are intuitively more typical than those at its boundary (Rodriguez and Laio, 2014), yet global centrality may assign them similar scores. Finally, traditional notions are tied to hand-crafted formulas and Euclidean geometry, making them difficult to apply directly to modern data types such as images, text, or time series.

A related challenge concerns inference. For many classical depths, evaluating the depth of a new point requires recomputing its relation to the entire reference sample. This coupling prevents fast or real-time inference, since scoring a new point is essentially as expensive as recomputing depths for the full cloud. Only a few special cases, such as Mahalanobis depth, admit closed-form scoring, but these rely on restrictive distributional assumptions and often degrade in high dimensions. In contrast, a learnable model can be trained once and then score new points via a single forward pass, without revisiting the training data, which is an attractive property for large-scale or streaming applications.

These difficulties motivate a more flexible and learnable notion of centrality. In modern machine learning, there is growing interest in distinguishing typical from atypical samples (Swayamdipta et al., 2020), often operating in representation spaces learned by self-supervision (Chen et al., 2020) or by manifold-preserving methods such as UMAP (McInnes et al., 2018). In outlier detection, deep one-class models (Ruff et al., 2018) and transformation-based approaches (Bergman and Hoshen, 2020) demonstrate the value of adaptive, data-driven centrality. In parallel, score-based generative models (Song et al., 2021) and flow-matching techniques (Lipman et al., 2023) show that denoising objectives

can capture density-related information that scales more gracefully with dimensions than explicit density estimation. Together, these directions suggest that modern centrality should be data-driven, representation-aware, and capable of bridging global and local structures.

However, learning centrality faces a fundamental difficulty. There are no ground-truth labels declaring which points are “central” or “peripheral”. Centrality is inherently relative, and its meaning lies in comparing points, not in assigning them absolute labels. In the absence of labels, existing neural methods typically rely on indirect proxies such as reconstruction error or one-class objectives (Ruff et al., 2018; Bergman and Hoshen, 2020). These proxies capture certain aspects of the data geometry but may not align with depth-like notions, and they often emphasize a global one-class objective by pulling all points toward a single center, at the expense of local density structure.

Our first step is therefore to learn centrality directly from pairwise comparisons. Given two points and a chosen dissimilarity, we declare the one that is closer to the other samples to be more central. Aggregating such local preferences across many random anchors yields an anchor-free global ordering, in the spirit of ranking and preference learning. This idea underlies our global centrality score. We learn a smooth scalar score on the representation space such that, for any two points, the difference between their scores, passed through a logistic sigmoid, approximates the probability that one would be judged more central than the other when both are compared to random reference points. Conceptually, this learned score acts as a neural analogue of an integrated dissimilarity-based depth.

Global rankings alone are not sufficient, however. Local density structure is crucial for identifying atypical points within clusters or along decision boundaries (Foorthuis, 2021; Bouman et al., 2024). This motivates our second step. Exact nonparametric density estimation is notably difficult in high dimensions, but denoising score matching and related techniques have shown that the gradient of a smoothed log-density is often more stable and learnable than the density itself (Hyvärinen and Dayan, 2005; Vincent, 2011; Song et al., 2021). Intuitively, the score field points towards regions of higher probability and can be viewed as an arrow pointing “inward” in the local geometry. When parameterized as the gradient of a scalar potential, this field can be integrated into a function that behaves like a local centrality measure.

We introduce Fused Unified centrality Score Estimation (FUSE), a neural framework for learning centrality across general data types. FUSE operates on fixed representations, and a shared encoder maps these representations to latent features, on top of which we attach two complementary heads. One is a global head, trained via pairwise ranking to approximate an integrated, anchor-free notion of centrality, and the other one is a local head, trained with denoising score matching to approximate a smoothed log-density potential in the latent space. Both heads operate in the same representation space and are calibrated onto a common $[0, 1]$ scale to make their outputs comparable. A homotopy module $f(x, t)$, indexed by $t \in [0, 1]$, then interpolates between the two signals, providing a single interpretable knob that balances global robustness and local sensitivity.

Our contributions are as follows. (1) We propose FUSE, a neural centrality framework that combines a ranking-based global signal with a score-based local signal. (2) We introduce a continuous family of centrality scores $f(x, t)$ parameterized by $t \in [0, 1]$, providing a clear and interpretable balance between robustness to global structure and sensitivity to local density. (3) We show empirically that FUSE recovers classical depth behavior in simple settings while extending naturally to non-Euclidean and high-dimensional data through pretrained encoders. (4) Once trained, FUSE scores new points in a single forward pass without revisiting the training samples, enabling fast centrality evaluation suitable for large-scale and streaming scenarios. (5) Through extensive experiments, we demonstrate that varying t uncovers structures missed by purely global centrality, yields interpretable orderings in synthetic and real data, and attains competitive outlier detection performance against strong classical baselines.

We use the term “centrality” informally. FUSE does not enforce all axioms of classical depth (Zuo and Serfling, 2000), but it retains two key features. Each point is assigned a scalar score, and sorting the sample by their scores induces a one-dimensional ordering that we interpret as going from more central to more outlying points, and any strictly increasing transformation of this score yields the same ranking and level sets. Meanwhile, FUSE extends depth-like ideas to modern, high-dimensional, and non-Euclidean data through representation learning.

The remainder of the paper is organized as follows. Section 2 introduces our neural centrality model and the FUSE model construction. Section 3 presents experiments on synthetic data and real datasets across images, time series, and text, followed by outlier detection tasks. We conclude the paper in Section 4. Additional experimental results and implementation details are provided in the Supplementary Material. A Python implementation of FUSE, together with scripts to reproduce examples, is available at <https://github.com/vuminhducvmd/FUSE>.

2 Method

We aim to learn a scalar centrality score for each point that smoothly interpolates between a global notion of centrality and a local, density-driven notion. Intuitively, points with high centrality lie in dense or central regions, whereas points with low centrality lie in sparse or boundary regions and may behave as outliers.

2.1 Neural centrality model

Let \mathcal{X} be a data space, and suppose we observe i.i.d. random elements $X_1, \dots, X_n \in \mathcal{X}$ with a common distribution. We write $\mathcal{X}_n := \{X_1, \dots, X_n\}$ for the observed sample. We start from a fixed representation map

$$\psi : \mathcal{X} \rightarrow \mathbb{R}^p,$$

and define

$$Z_i = \psi(X_i) \in \mathbb{R}^p, \quad i = 1 \dots, n$$

as the latent representation of X_i , where p is the representation dimension and may vary across architectures. The map ψ can be the identity on raw Euclidean data, or a pretrained feature extractor such as CLIP for images (Radford et al., 2021), BERT for text (Devlin et al., 2019), or SimCLR for visual embeddings (Chen et al., 2020). In all experiments, ψ is kept fixed and is not updated during training, while all trainable parameters reside in the subsequent shared encoder and the global and local heads.

We equip the representation space \mathbb{R}^p of $\psi(X)$ with a dissimilarity measure $\delta_Z : \mathbb{R}^p \times \mathbb{R}^p \rightarrow [0, \infty)$, and compute dissimilarities between raw data points via their representations by defining $\delta(X_i, X_j) = \delta_Z(\psi(X_i), \psi(X_j))$. For Euclidean data with ψ equal to the identity map, this reduces to applying δ_Z directly in the original input space. For non-Euclidean data such as images, text, or time series, dissimilarities can be evaluated in the representation space through ψ .

On top of the fixed latent representation $\psi(x)$ for $x \in \mathcal{X}$, we place a shared encoder $e_{\theta_e} : \mathbb{R}^p \rightarrow \mathbb{R}^q$, followed by two scalar heads with parameters θ_g and θ_l . For a generic input x , we first compute $\psi(x)$ and $e_{\theta_e}(\psi(x))$, and then define the global and local heads as

$$g_{\theta}(\psi(x)) = h_g(e_{\theta_e}(\psi(x)); \theta_g) \in \mathbb{R}, \quad l_{\theta}(\psi(x)) = h_l(e_{\theta_e}(\psi(x)); \theta_l) \in \mathbb{R}.$$

Here $\theta = (\theta_e, \theta_g, \theta_l)$ collects all trainable parameters of the shared encoder and the two heads. For notational simplicity we write g_{θ} and l_{θ} to denote the resulting global and local scoring functions.

The global head g_{θ} is trained to produce an anchor-free ranking that aligns with pairwise centrality comparisons, capturing coarse, cross-cluster structure. The local head l_{θ} is trained via denoising score matching (DSM) (Hyvärinen and Dayan, 2005; Vincent, 2011) so that its gradient approximates the score of a Gaussian-smoothed version of the data distribution in representation space, capturing density-driven local typicality. In Section 2.2 we introduce a homotopy module $f(x, t)$, $t \in [0, 1]$, that interpolates between these two calibrated signals to yield a continuous family of centrality scores controlled by a single parameter t .

2.1.1 GLOBAL HEAD: ANCHOR-MARGINAL RANKING

The global head learns an anchor-free centrality score $g_{\theta}(\psi(x))$ such that points closer to the majority of the data receive larger scores. Our starting point is that centrality is inherently comparative. Given two candidates $x_1, x_2 \in \mathcal{X}$ and a reference point $x_0 \in \mathcal{X}$, we can say which one is more central relative to x_0 based on distances under δ , even though we do not observe absolute labels.

For an anchor x_0 and candidates x_1, x_2 , we define the binary relation

$$x_1 \prec_{x_0} x_2 \iff \delta(x_1, x_0) < \delta(x_2, x_0),$$

meaning that, relative to x_0 , x_1 is more central than x_2 if it is closer in the representation space. This comparison rule is deterministic given (x_0, x_1, x_2) . To remove the dependence on any particular anchor, we marginalize over the random anchor X_0 . For a fixed pair $(x_1, x_2) \in \mathcal{X} \times \mathcal{X}$, we define the marginal preference probability

$$\pi(x_1, x_2) := \Pr [x_1 \prec_{X_0} x_2],$$

which is the probability that x_1 is judged more central than x_2 when compared to a random reference point X_0 .

In practice, we approximate this probability using a finite anchor set $S_0 \subset \mathcal{X}_n$. At each epoch we partition the sample into an anchor set S_0 and two candidate sets S_1, S_2 , and draw a moderate collection of candidate pairs $\mathcal{S}_{12} \subset S_1 \times S_2$. For each $(x_1, x_2) \in \mathcal{S}_{12}$ we then estimate

$$\hat{\pi}(x_1, x_2) = \frac{1}{|\mathcal{A}_{12}|} \sum_{x_0 \in \mathcal{A}_{12}} \mathbf{1}\{x_1 \prec_{x_0} x_2\},$$

where $\mathcal{A}_{12} \subset S_0$ is a subset of anchors and $|\cdot|$ denotes cardinality. This partitioned scheme greatly reduces the cost of computing preferences while still providing a rich set of comparisons. Concrete sampling choices and further variants are described in Section 2.3 and Supplement S2.

To map empirical preference probabilities to a scalar score, we adopt the Bradley–Terry (BT) model for paired comparisons (Bradley and Terry, 1952). The BT model assumes that each item x has a one-dimensional latent score $g_\theta(\psi(x))$ and that the probability of x_1 being preferred to x_2 is a logistic function of the score difference

$$\Pr [x_1 \text{ preferred to } x_2] \approx \sigma(g_\theta(\psi(x_1)) - g_\theta(\psi(x_2))),$$

where $\sigma(u) = (1 + e^{-u})^{-1}$ is the logistic sigmoid. In our setting, “preferred” means “judged more central than” when compared via random anchors. Thus $g_\theta(\psi(x))$ can be interpreted as a global centrality score, and larger $g_\theta(\psi(x))$ means that x tends to win more comparisons against other points.

We train g_θ by minimizing the cross-entropy between the empirical preference $\hat{\pi}(x_1, x_2)$ and the BT model prediction,

$$\begin{aligned} \mathcal{L}_{\text{global}}(\theta) = \mathbb{E}_{(X_1, X_2)} \Big[& -\hat{\pi}(X_1, X_2) \log \sigma(g_\theta(\psi(X_1)) - g_\theta(\psi(X_2))) \\ & - (1 - \hat{\pi}(X_1, X_2)) \log (1 - \sigma(g_\theta(\psi(X_1)) - g_\theta(\psi(X_2)))) \Big], \end{aligned} \quad (1)$$

and the expectation is approximated by the empirical average over \mathcal{S}_{12} . For each pair $(x_1, x_2) \in \mathcal{S}_{12}$, $\hat{\pi}(x_1, x_2)$ is the fraction of anchors that consider x_1 more central than x_2 , while $\sigma(g_\theta(\psi(x_1)) - g_\theta(\psi(x_2)))$ is the model’s predicted probability. The loss encourages $g_\theta(\cdot)$ to preserve these integrated orderings of centrality.

Anchors are used only to construct supervision during training. After marginalization, the resulting score $g_\theta(\psi(x))$ depends solely on x and can be evaluated independently at inference time via a single forward pass, yielding an anchor-free global centrality score whose pairwise differences approximate integrated depth-like preferences.

2.1.2 LOCAL HEAD: DENOISING SCORE MATCHING

The global head describes how a point behaves with respect to the dataset as a whole and mainly captures coarse, cross-cluster structure. In clustered data, we often observe that points from the same cluster receive similar global scores even when one lies near the cluster center and another near the boundary, so the global score is less sensitive to fine within-cluster differences. This role is similar to that of classical global depth functions, which provide a center-outward ordering for the full distribution but are not designed to capture local, cluster-specific structure (Agostinelli and Romanazzi, 2011; Francisci et al., 2023). For tasks such as outlier detection within clusters, we therefore also need a notion of local centrality that is sensitive to nearby density (Bouman et al., 2024), in line with local depth constructions and local-density based outlier methods such as local outlier factor (Breunig et al., 2000) and cluster-based local outlier detection (He et al., 2003).

A natural way to formalize local centrality is through the density of the representation. Recall $Z = \psi(X)$ and let p_Z be its density function. Points in regions where p_Z is large are more central locally. Directly estimating p_Z is difficult in high dimensions, but score-based methods circumvent this by focusing on the gradient of a smoothed log-density, which is typically more stable and learnable than the density itself (Hyvärinen and Dayan, 2005; Vincent, 2011; Song et al., 2021). The resulting score field points towards regions of higher probability and therefore encodes how typical a point is within its local neighborhood.

For a noise scale $\eta > 0$, we define the Gaussian-smoothed density

$$p_{Z,\eta}(z) := (p_Z * \varphi_\eta)(z), \quad s_\eta(z) := \nabla_z \log p_{Z,\eta}(z),$$

where φ_η is the density of $\mathcal{N}(0, \eta^2 I_p)$ and $*$ denotes convolution. We parameterize a scalar potential $l_\theta : \mathbb{R}^p \rightarrow \mathbb{R}$ and define the model score

$$s_\theta(z) := \nabla_z l_\theta(z),$$

which is meant to approximate $s_\eta(z)$.

Denoising score matching (DSM) (Vincent, 2011) provides a principled and scalable way to train this model. Consider the joint density of a pair (z, \tilde{z}) ,

$$q_\eta(z, \tilde{z}) = p_Z(z) \varphi_\eta(\tilde{z} - z).$$

Let $(Z, \tilde{Z}) \sim q_\eta$ and write $q_\eta(\tilde{z}|z)$ as the corresponding conditional density. Following Vincent (2011, Eq. (9)), the DSM objective for a score field $s_\theta(\tilde{z})$ can be written as

$$\mathcal{L}_{\text{local}}(\theta) = \frac{1}{2} \mathbb{E}_{(Z, \tilde{Z})} [\|s_\theta(\tilde{Z}) - \partial_{\tilde{z}} \log q_\eta(\tilde{Z} | Z)\|_2^2].$$

For Gaussian corruption, Vincent (2011, Eq. (10)) shows that $\partial_{\tilde{z}} \log q_\eta(\tilde{z} | z) = \eta^{-2}(z - \tilde{z})$. Writing $\varepsilon := \tilde{Z} - Z$, then we have $\partial_{\tilde{z}} \log q_\eta(\tilde{Z} | Z) = -\eta^{-2}\varepsilon$, and we obtain the equivalent form

$$\mathcal{L}_{\text{local}}(\theta) = \frac{1}{2} \mathbb{E}_{(Z, \varepsilon)} [\|s_\theta(Z + \varepsilon) + \eta^{-2}\varepsilon\|_2^2], \quad (2)$$

where Z and $\varepsilon \sim \mathcal{N}(0, \eta^2 I_p)$ are independent. In implementation, the expectation in equation 2 is approximated by averaging over the training representations $\{Z_i\}_{i=1}^n$ and a small number of Gaussian noise samples per point, with details in Section 2.3. Minimizing $\mathcal{L}_{\text{local}}$ over a sufficiently rich class encourages s_θ to approximate the smoothed score s_η (Hyvärinen and Dayan, 2005; Vincent, 2011), so that l_θ behaves like a smoothed log-density up to an additive constant. We therefore interpret $l_\theta(z)$ as a local centrality function. Larger values indicate that z lies in a region where the smoothed density $p_{Z, \eta}$ is high, while smaller values correspond to boundary or low-density regions.

On the sample $\{Z_i\}_{i=1}^n$, we define the empirical local centrality score as

$$f_l(X_i) := \text{Normalize}(l_\theta(Z_i)),$$

where the function $\text{Normalize}(\cdot)$ maps values to $[0, 1]$, and details can be seen in Section 2.2. This construction can be viewed as a learned, high-dimensional analogue of Gaussian kernel density estimation (Parzen, 1962; Silverman, 2018). Instead of explicitly summing kernels around each point, DSM learns a parametric potential l_θ whose gradient matches the smoothed score field s_η . The resulting model is teacher-free, efficient at inference, and complements the global head by capturing fine-grained, density-driven typicality.

2.2 FUSE: homotopy centrality interpolation

The global and local heads provide two complementary centrality signals, but their raw outputs live on different scales and are not directly comparable. To put them on a common scale and expose a single interpretable control over their relative influence, we first calibrate both outputs to the interval $[0, 1]$ and then combine them via a homotopy.

For the global head, $g_\theta(\psi(x))$ plays the role of a BT logit. Since the training loss is logistic, applying a sigmoid transformation

$$f_g(X) = \sigma(g_\theta(\psi(X)))$$

is natural, since it maps $g_\theta(\psi(X))$ to $[0, 1]$ and yields a probability-like global centrality score. Any strictly increasing transformation would induce the same ranking, but $\sigma(\cdot)$ is numerically stable and interpretable.

For the local head, $l_\theta(\psi(X))$ serves as a surrogate smoothed log-density up to an additive constant. Because such log-densities can be shifted arbitrarily, we normalize $l_\theta(X)$ empirically. Let $q_{0.01}$ and $q_{0.99}$ denote the empirical 1st and 99th percentiles of $\{l_\theta(\psi(X_i))\}_{i=1}^n$ on the training set. We define the local centrality score

$$f_l(X) = \min\left\{1, \max\left\{0, \frac{l_\theta(\psi(X)) - q_{0.01}}{q_{0.99} - q_{0.01}}\right\}\right\},$$

which linearly rescales $l_\theta(\psi(X))$ between these quantiles and clips extreme values. This normalization makes the local scores comparable to the global scores and robust to outliers. During inference, $q_{0.01}$ and $q_{0.99}$ are kept fixed.

We then form the homotopy centrality score by linear interpolation,

$$f(X, t) = (1 - t) f_g(X) + t f_l(X), \quad t \in [0, 1].$$

The parameter t controls the balance between the two signals: $t = 0$ yields a purely global centrality score, $t = 1$ yields a purely local one, and intermediate values provide mixtures of global and local behavior. We adopt linear interpolation for simplicity and interpretability, while other schedules are also possible.

2.3 Training

The overall training alternates between the global pairwise-ranking loss equation 1 and the local DSM loss equation 2, allowing the model to capture both coarse global structure and fine-grained local density. The workflow is summarized in Figure 1, and detailed pseudocode is given in Algorithm 1.

During training, the global ranking loss equation 1 is implemented using the partitioned sampling scheme introduced in Section 2.1.1. At each epoch, we construct three disjoint subsets (S_0, S_1, S_2) of \mathcal{X}_n to approximate the expectations in equation 1. Specifically, we randomly split the sample into an anchor set S_0 and two candidate sets S_1 and S_2 of (approximately) equal size. From S_1 and S_2 , we sample $\lfloor n/3 \rfloor$ pairs (x_1, x_2) to compose S_{12} , and for each pair, sample a small number of anchors (64 in our experiments) from S_0 to estimate the empirical preference $\hat{\pi}(x_1, x_2)$. This partitioned scheme provides a good trade-off between computational cost and performance, yielding comparable accuracy with substantially lower time complexity. Alternative sampling strategies and comparisons are discussed in Supplement S2.

Jointly, the local potential l_θ is optimized using DSM. At each epoch, for each representation Z_i we generate a fixed number 8 of Gaussian perturbations to approximate the expectation in equation 2 and update the model using the resulting noisy batch. In our synthetic and first four real data experiments we fix the noise scale at $\eta = 1$, while in the

Algorithm 1: TRAINING: Joint training of global and local centrality heads

Input : Sample $\mathcal{X}_n = \{X_i\}_{i=1}^n$; representation map ψ ; dissimilarity δ_Z ; number of epochs T ; DSM noise scale $\eta > 0$; number of DSM resamples per epoch $R \in \mathbb{N}$; optimizer \mathcal{O} .

Output: Trained global and local heads g_θ and l_θ .

// Precompute representations and induced dissimilarity

Define $\delta(X_i, X_j) := \delta_Z(\psi(X_i), \psi(X_j))$ for use below.

for $epoch \leftarrow 1$ **to** T **do**

 Randomly split \mathcal{X}_n into three disjoint subsets S_0, S_1, S_2 .

 // Global head: anchor-marginal ranking

 Sample a set of candidate pairs $\mathcal{S}_{12} \subset S_1 \times S_2$ of size $\lfloor n/3 \rfloor$.

foreach $(X_i, X_j) \in \mathcal{S}_{12}$ **do**

 Sample a small anchor set $\mathcal{A}_{ij} \subset S_0$.

 Set $\hat{\pi}(X_i, X_j)$ to the fraction of anchors $X_0 \in \mathcal{A}_{ij}$ such that $\delta(X_i, X_0) < \delta(X_j, X_0)$.

 Compute the global loss $\mathcal{L}_{\text{global}}(\theta)$ using equation 1 with pairs (X_i, X_j) and labels $\hat{\pi}(X_i, X_j)$, and update θ with optimizer \mathcal{O} .

if $R > 0$ **then**

 // Local head: denoising score matching

for $r \leftarrow 1$ **to** R **do**

for $i \leftarrow 1$ **to** n **do**

 Set $Z_i \leftarrow \psi(X_i)$, draw $\varepsilon_i \sim \mathcal{N}(0, \eta^2 I_p)$, and form noisy input $\tilde{Z}_i \leftarrow Z_i + \varepsilon_i$.

 Compute scores $s_\theta(\tilde{Z}_i) = \nabla_z l_\theta(z)|_{z=\tilde{Z}_i}$ and the empirical DSM loss $\mathcal{L}_{\text{local}}(\theta)$ from equation 2, then update θ with optimizer \mathcal{O} .

 Compute calibration quantiles $q_{0.01}, q_{0.99}$ from $\{l_\theta(\psi(X_i))\}_{i=1}^n$ on the training set and fix them for inference.

Algorithm 2: INFERENCE: Interpolated homotopy centrality score

Input : New point X_{new} ; homotopy parameter $t \in [0, 1]$; representation map ψ ; heads g_θ, l_θ ; calibration quantiles $q_{0.01}, q_{0.99}$.

Output: Interpolated centrality $f(X_{\text{new}}, t)$.

Compute global score $f_g(X_{\text{new}}) \leftarrow \sigma(g_\theta(\psi(X_{\text{new}})))$.

Compute local score

$$f_l(X_{\text{new}}) \leftarrow \min \left\{ 1, \max \left\{ 0, \frac{l_\theta(\psi(X_{\text{new}})) - q_{0.01}}{q_{0.99} - q_{0.01}} \right\} \right\}.$$

Return interpolated centrality

$$f(X_{\text{new}}, t) \leftarrow (1 - t)f_g(X_{\text{new}}) + tf_l(X_{\text{new}}).$$

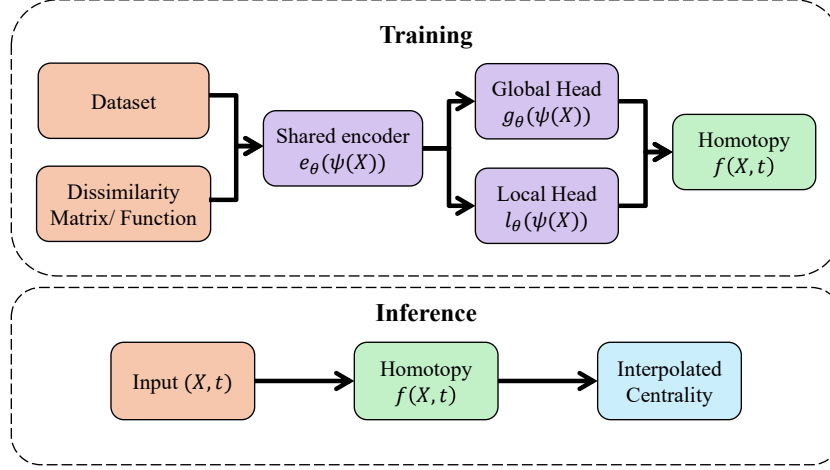


Figure 1: Training (top): mapped data $\psi(X)$ pass through a shared encoder and branch into global g_θ and local l_θ heads. Inference (bottom): given (X, t) , the homotopy outputs a single centrality score $f(X, t)$. The dissimilarity δ can be defined on raw data or pretrained embeddings.

outlier-detection benchmarks we treat η as a tuning parameter. The numbers $\lfloor n/3 \rfloor$, 64, and the number of DSM resamples per epoch are chosen for illustration. When time and computational resources permit, increasing these values yields more accurate Monte Carlo estimates of the underlying expectations.

After training, we fix the network parameters θ and the calibration constants $q_{0.01}, q_{0.99}$ estimated on the training set, and we do not update them during inference. Given any new point X_{new} , FUSE computes its global score $f_g(X_{\text{new}})$ and local score $f_l(X_{\text{new}})$ via a single forward pass followed by the fixed normalization in Section 2.2, and then evaluates $f(X_{\text{new}}, t)$ for any $t \in [0, 1]$. The detailed pseudocode is given in Algorithm 2. In contrast to many classical depth functions that must recompute a point’s relation to the entire reference sample, FUSE performs fast inference. Once training is complete, scoring new points requires no access to the training data and no further optimization, making the method well suited to large-scale or streaming applications.

Finally, all experiments use a small shared encoder feeding the two scalar heads g_θ and l_θ , and the architecture choices for each dataset are summarized in Supplement S1.

3 Experiments

We evaluate FUSE on synthetic and real-world datasets to assess three key questions: (i) whether the learned scores reproduce qualitative behaviors expected from classical centrality or depth notions; (ii) whether the homotopy parameter $t \in [0, 1]$ provides an interpretable interpolation between global and local structure; and (iii) whether FUSE achieves compet-

itive performance on outlier detection benchmarks. Notably, $t=0$ corresponds to the global regime (Global) and $t=1$ corresponds to the local regime (Local).

We begin with controlled synthetic experiments to examine qualitative behavior and monotonicity. We then visualize FUSE on three representative modalities, including images, time series, and text, to illustrate how t reveals multi-scale structures. Finally, we evaluate FUSE and its global and local components on two outlier detection benchmarks.

3.1 Synthetic data

Our synthetic experiments test whether FUSE recovers the expected center-outward behavior on standard distributions and whether the homotopy parameter yields a smooth transition from global to local structures.

For illustration, each setting contains $n = 5000$ i.i.d. samples in two dimensions. In the Gaussian setting we draw $X \sim \mathcal{N}(0, \Sigma)$, where the covariance matrix $\Sigma \in \mathbb{R}^{2 \times 2}$ is a random symmetric positive-definite matrix generated by `sklearn.datasets.make_spd_matrix`. For the Student- t case we sample each coordinate independently from a centered t_{10} distribution, and for the Uniform case we sample each coordinate independently from $\text{Unif}(-2, 2)$. For such unimodal families, we expect: (i) points near the center to receive larger centrality values; (ii) scores decrease monotonically as we move outward; and (iii) high correlation between centrality and Euclidean distance to the population center. We use these settings to assess how the homotopy scores $f(x, t)$ capture classical depth-like behavior. We next consider a multimodal setting using a Gaussian mixture with four components. Global centrality should emphasize coarse, cross-cluster structure, assigning similar values within each component, and local behavior should highlight cluster boundaries and mode-specific density. By sweeping t from 0 to 1, we examine whether FUSE progressively resolves individual clusters while preserving global structure. Euclidean distances are used to construct the FUSE model.

Figure 2 shows the learned homotopy centrality surfaces for $t \in \{0, 0.25, 0.5, 0.75, 1\}$. For Gaussian and Student- t distributions, centrality peaks at the mean and decays smoothly outward, matching elliptical level sets of the density. For the Uniform distribution, although the density is constant, FUSE still learns a meaningful notion of center versus boundary. For the Gaussian mixture, t creates a smooth path from a global basin spanning all components to mode-specific local structure. These behaviors align closely with the intuition behind classical depth.

We compare Global and Local against classical centrality measures, including Kernel Density Estimation (KDE; Parzen 1962), Mahalanobis depth (MAH; Mahalanobis 1936), potential depth (POT; Pokotylo and Mosler 2019), projection depth (PRO; Zuo and Serfling 2000), spatial depth (SPA; Vardi and Zhang 2000) and Tukey depth (Tukey; Tukey 1975). All methods are implemented following their reference descriptions and parameters as described in Supplement S3. Since the scales of different methods’ outputs are not directly comparable, we focus on rank-based metrics and compute Spearman’s and Kendall’s rank

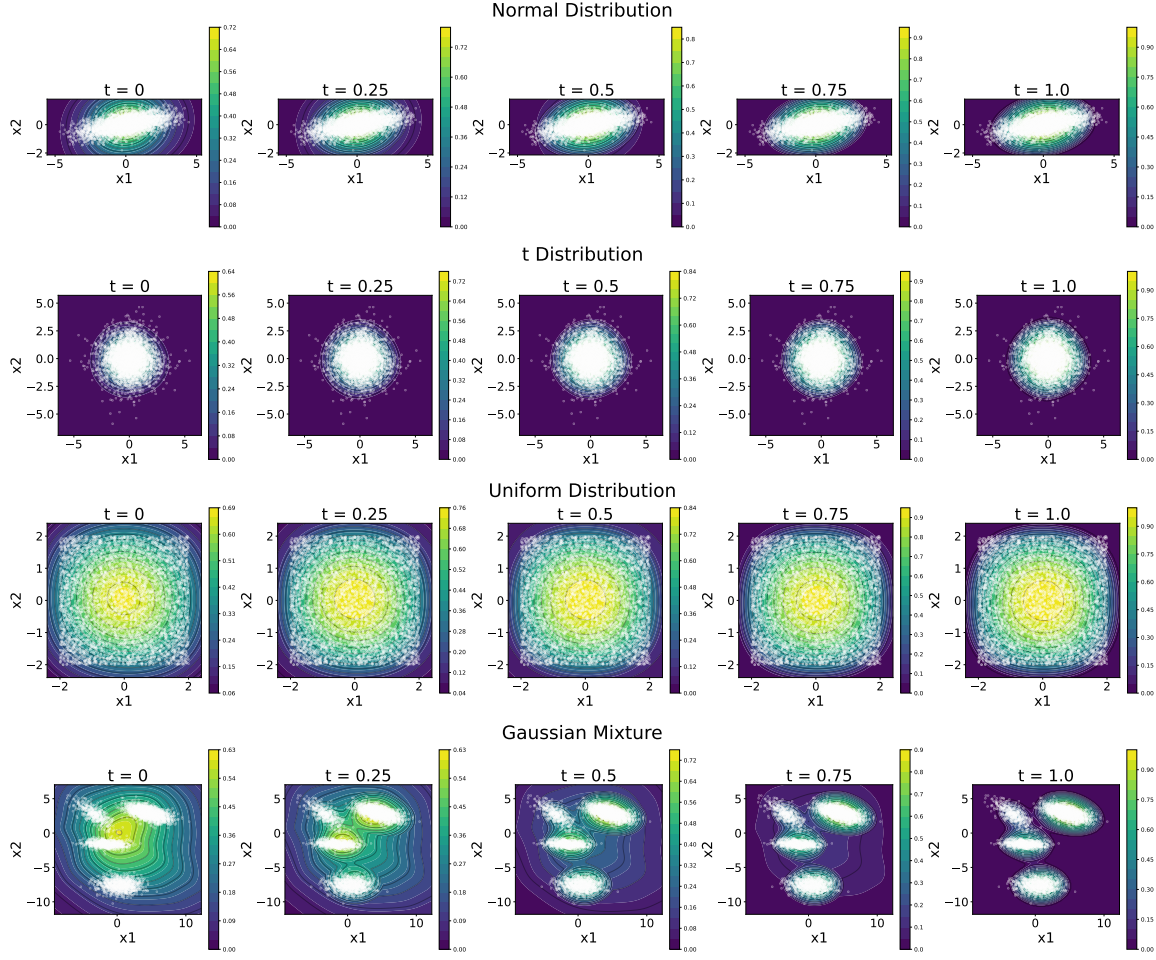


Figure 2: From top to bottom: Homotopy centrality contours on Normal, Student- t , Uniform, Gaussian mixture. $t \in \{0, 0.25, 0.5, 0.75, 1\}$.

correlations (Spearman, 1904; Kendall, 1938) between the learned centrality scores and the Euclidean distance to the mean.

Table 1 reports these correlations. Both Global and Local achieve the highest or near-highest values on the unimodal settings, with Spearman and Kendall correlations typically above 0.95, demonstrating a strong monotone alignment with the ground-truth structure. The mixture example further highlights FUSE’s flexibility. By varying t , FUSE smoothly transitions from a global to a local centrality view.

Inference for FUSE requires only a single forward pass, offering substantial advantages in efficiency over classical depth functions in both low and high dimensions. Figure 3 reports the inference time per sample for all methods on Gaussian, Student- t , and Uniform distributions, with FUSE evaluated using a single unified model where Global and Local are trained jointly. For each setting, we measure how long it takes to compute scores

Table 1: Rank correlations between centrality and Euclidean distance to the mean.

Data	Metric	Global	Local	KDE	MAH	POT	PRO	SPA	Tukey
Normal	Spearman	0.996	0.982	0.981	0.781	0.999	0.776	0.993	0.782
	Kendall	0.951	0.894	0.894	0.603	0.981	0.598	0.940	0.605
Student- t	Spearman	0.998	0.999	1.000	1.000	1.000	0.999	1.000	1.000
	Kendall	0.964	0.980	0.992	0.991	0.997	0.977	0.990	0.982
Uniform	Spearman	0.998	0.998	0.998	1.000	1.000	0.988	0.999	0.989
	Kendall	0.966	0.961	0.962	0.984	0.966	0.915	0.970	0.926

for all n data points and then divide this total time by n . The curves show this average time per sample. Across all settings, the inference time per sample of FUSE stays in the microsecond range, about 10^{-6} – 10^{-5} seconds, whereas classical depth functions such as KDE, POT, PRO, SPA, and Tukey typically require 10^{-4} – 10^{-2} seconds per sample. Thus FUSE is roughly two to four orders of magnitude faster at inference. When the sample size is fixed at $n = 500$ and the dimension increases, this gap widens further. When the dimension is fixed at $d = 5$ and the sample size increases, inference time per sample grows for all classical methods, while FUSE and MAH remain nearly flat. Moreover, FUSE matches MAH in speed while being more robust and broadly applicable across data types.

3.2 Real data exploration

We next evaluate whether our centrality can reveal meaningful geometric structure in real, high-dimensional or non-Euclidean datasets. We consider three representative modalities, including images, time series and text, and study how the homotopy parameter $t \in [0, 1]$ provides interpretable transitions between global and local views. These experiments complement the synthetic results and demonstrate that FUSE can serve as a simple, unified tool for exploring complex datasets.

All datasets follow a common process. We begin with either raw data or pretrained embeddings, followed by normalization when appropriate. From these representations, we compute a pairwise distance matrix using a task-suitable metric and train our neural centrality model based on this distance information. For visualization, we embed the learned centrality values into two dimensions using UMAP (McInnes et al., 2018) and examine how the resulting plots evolve as t increases from 0 to 1.

Across all datasets, two consistent advantages emerge. First, FUSE highlights intrinsic organization within each modality, revealing clusters, gradients, and atypical samples that are difficult to identify in raw representation space. Second, the homotopy parameter t provides a smooth and transparent way to shift emphasis from broad global structure ($t=0$) to fine-grained local density ($t=1$). Together, these findings suggest that FUSE provides an interpretable multi-scale summary of a dataset’s geometry.

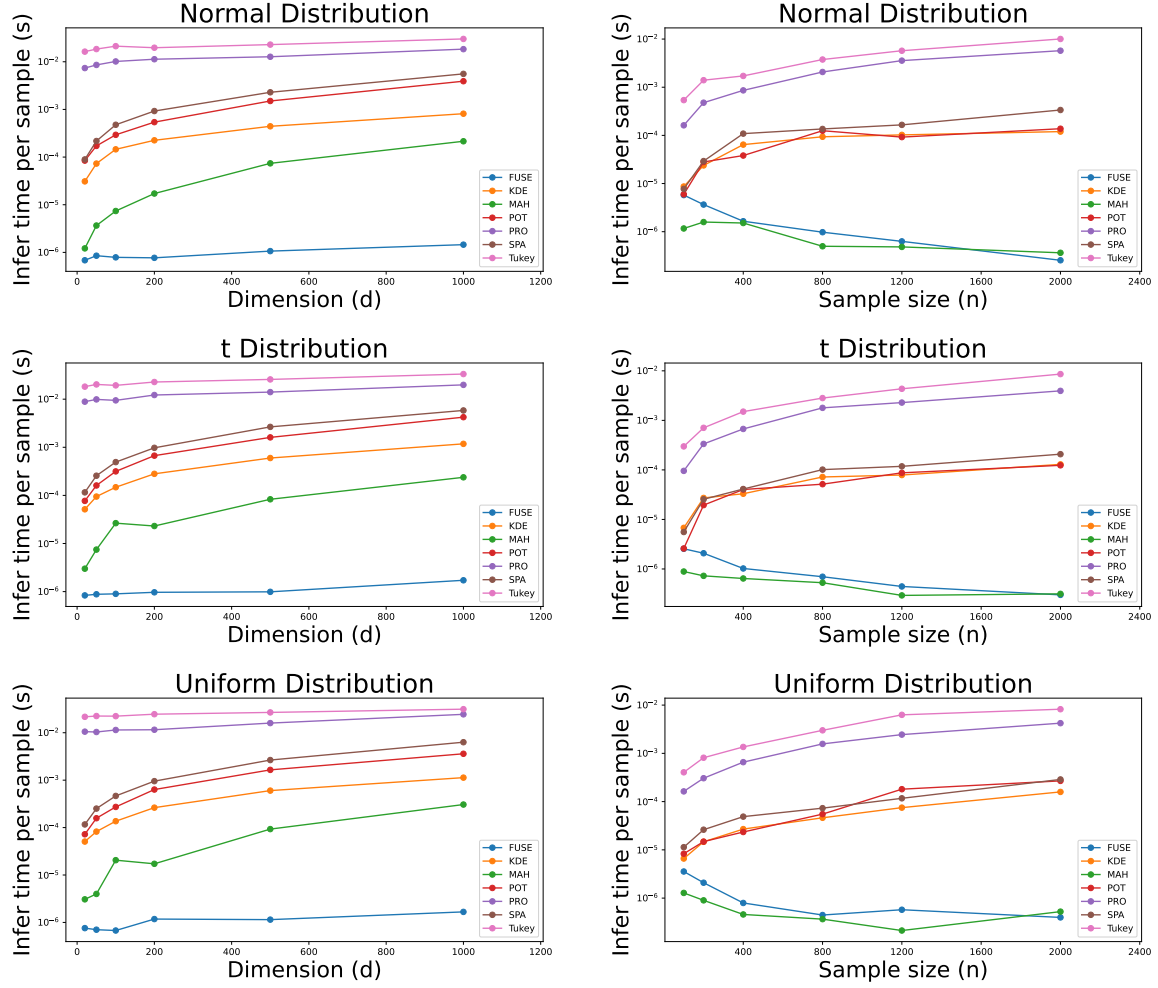


Figure 3: Inference time per sample comparison of methods across increasing dimensions (left) and increasing sample sizes (right).

3.2.1 IMAGES: CIFAR-10

We first analyze the **airplane** class of CIFAR-10 (Krizhevsky et al., 2009), which contains 60,000 color images across ten object classes. For visualization, we sample $n = 1000$ airplane images and represent each image using a 512-dimensional CLIP embedding (Radford et al., 2021).

All distances, graphs and baseline depth methods in this subsection are applied in the representation space. We focus on Global and classical depth-style baselines, including POT, PRO, MAH, SPA and Tukey, using the same configurations as in Section 3.1 (see Supplement S3 for implementation details). We do not include KDE or Local here, because these methods are designed to highlight very local density peaks rather than to produce a single smooth center-outward ordering. On the CIFAR-10 CLIP graph, this leads to many

sharp changes in their scores between nearby neighbors, so the graph-smoothness measure (introduced below) would mainly reflect this intended local variability instead of the quality of the method.

To assess how smoothly centrality varies across the data manifold, we construct a symmetrized 10-nearest-neighbor graph from the embeddings. Let W be the adjacency matrix, and let D be the diagonal degree matrix with $D_{ii} = \sum_j W_{ij}$. The graph Laplacian is defined as $L = D - W$. Given centrality scores $s \in \mathbb{R}^n$, we evaluate smoothness using the normalized quadratic form

$$\frac{s^\top L s}{\|s\|_2^2} = \frac{1}{2\|s\|_2^2} \sum_{i,j} W_{ij} (s_i - s_j)^2,$$

which measures how much the scores vary across adjacent nodes (Dong et al., 2016). Lower values indicate that neighboring points have more similar centrality, reflecting smoother structure. Because classical depth methods output scores on different scales, all methods use min–max normalization to $[0, 1]$ before evaluation.

Table 2: Inference time per sample and graph smoothness on CIFAR-10 (airplane).

Metric	Global	MAH	POT	PRO	SPA	Tukey
Infer time per sample (ms)	0.003	0.224	18	17	96	25
Graph Smoothness	0.228	1.419	0.263	0.595	2.140	25.833

Table 2 shows that Global achieves the lowest graph-smoothness score (0.228) and the fastest inference time among all methods, indicating the most coherent variation across the CLIP manifold. POT attains a lower smoothness score than MAH, PRO, SPA, and Tukey, but is significantly slower at inference. PRO and Tukey rely on approximate implementations and exhibit high graph roughness on the CLIP manifold. For Tukey, this behavior matches its known degeneracy in high dimensions. Its true population depth collapses onto a nearly constant value for most points (Dutta et al., 2011; Yeon et al., 2025), so the remaining variation after min–max normalization is essentially numerical noise rather than meaningful geometric structure. Overall, Global provides the best balance of interpretability, stability, and computational efficiency.

Figure 4 displays UMAP visualizations for all methods’ results. Global produces scores that vary smoothly across the UMAP embedding. Nearby points have similar values and there is a clear trend from low to high centrality regions. POT is also relatively smooth while emphasizing several local high scores rather than a single dominant center. SPA and PRO exhibit more speckled, high-frequency variation, while MAH mainly reflects an approximately elliptical notion of centrality that does not match well the curved shape of the embedding. Tukey depth is almost constant, consistent with its high-dimensional

degeneracy. The remaining variation appears to be dominated by numerical noise rather than meaningful structures.

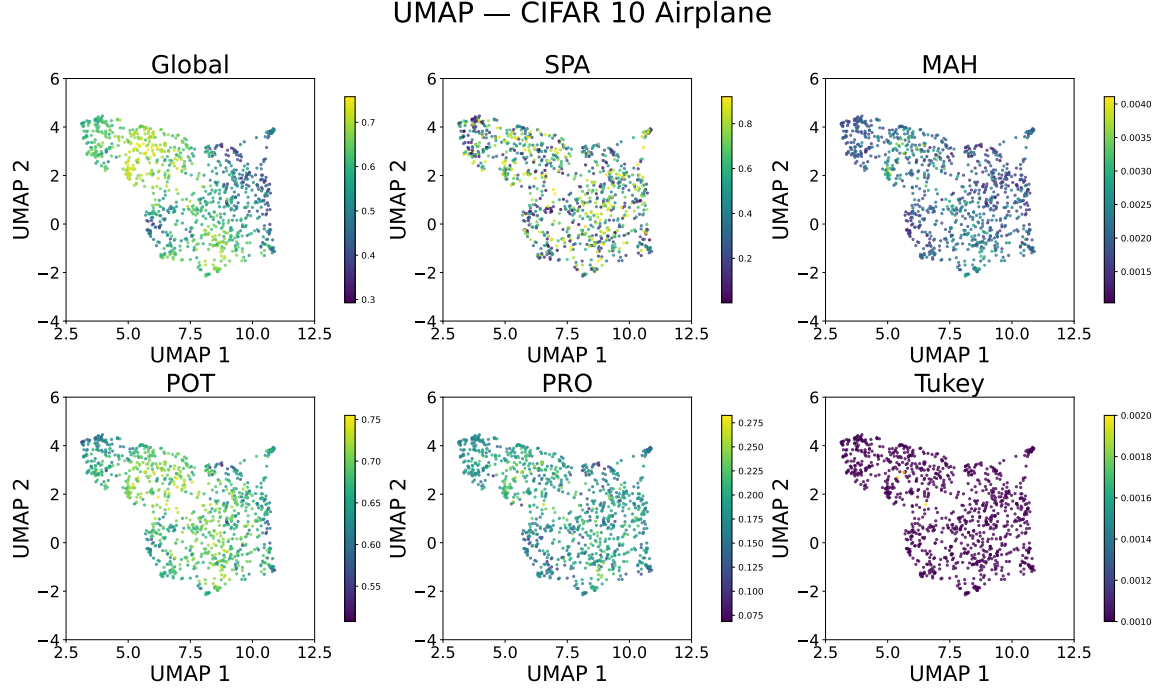


Figure 4: Comparison of centrality methods on CIFAR-10 (airplane).

3.2.2 IMAGES: MNIST

We next examine MNIST (LeCun et al., 2002). Each grayscale 28×28 image is flattened to a 784-dimensional vector. We use a fixed subset of 10,000 samples and compute their pairwise Euclidean distances for our model.

Figure 5 presents UMAP projections of the learned homotopy centrality. Clusters corresponding to the ten digits are visible even in the raw embedding, but FUSE provides a clearer interpretation. At $t=0$, global centrality captures inter-class structure. Digits such as 4, 7 and 9 overlap and exhibit relatively high centrality, while more distinctive digits, such as 0, 2 and 6, lie toward the periphery. As t increases, FUSE places more emphasis on local density. At $t=1$, the highest centrality values concentrate around the dense cores of each digit cluster, providing a refined within-cluster perspective.

This evolution illustrates how homotopy centrality connects global geometric relationships with local density within each cluster, offering a unified multi-scale view of the dataset.

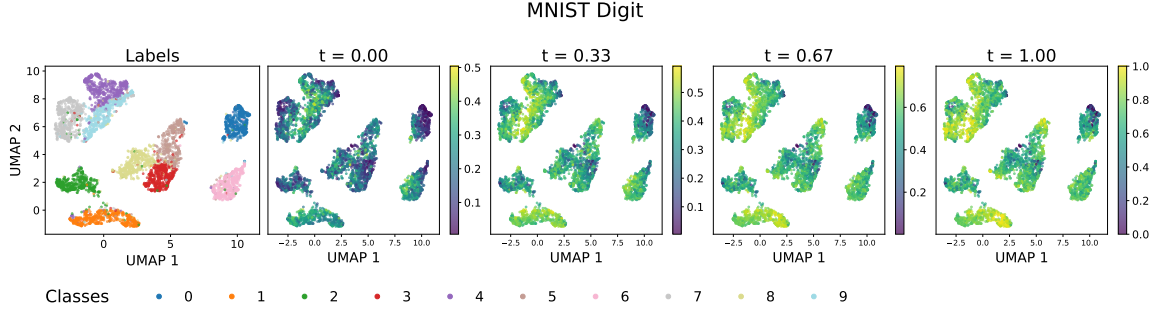


Figure 5: Homotopy centrality on MNIST.

3.2.3 TIME SERIES: FORDA

The FordA dataset (Dau et al., 2019) contains one-dimensional time series labeled into two classes. We represent each series using 22-dimensional `catch22` features (Lubba et al., 2019), which preserve essential temporal characteristics while enabling efficient distance computation. Euclidean distances in this feature space are used for training.

Figure 6 shows the UMAP projection colored by homotopy centrality. Because the two classes strongly overlap, global centrality ($t=0$) is nearly flat, capturing only weak global structure. As t increases, FUSE increasingly highlights local density variations. Dense clusters receive higher centrality, while scattered or boundary points receive lower values. By $t=1$, the local head captures boundaries that better align with class structure.

FordA demonstrates a scenario where local information is more informative than global geometry, and FUSE naturally adapts across this spectrum.

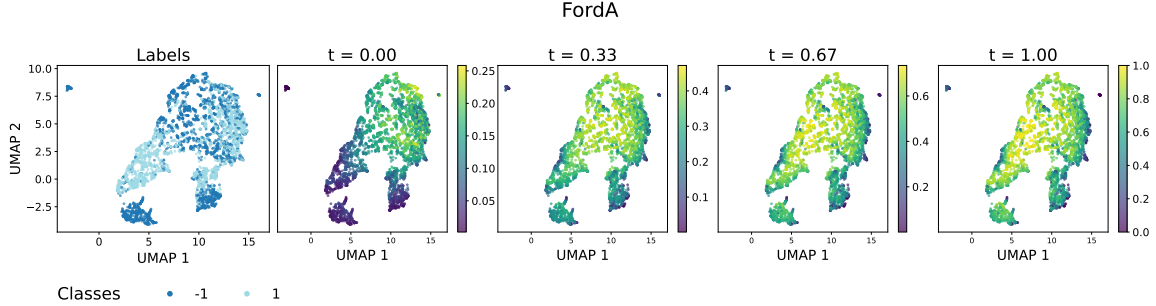


Figure 6: Homotopy centrality on FordA.

3.2.4 TEXT: TWEETVAL (SENTIMENT)

The TweetEval benchmark (Barbieri et al., 2020) contains Twitter datasets for several text classification tasks. In our experiment, we focus on the sentiment classification subset, which has three classes: negative (0), neutral (1), and positive (2), and for computational

efficiency we use a fixed subset of 1,000 tweets. Each tweet is embedded using the pooled [CLS] output from `distilbert-base-uncased-finetuned-sst-2-english` (Sanh et al., 2019; Socher et al., 2013). Pairwise cosine distances define the training metric.

Figure 7 shows the UMAP projection colored by homotopy centrality. Tweets with positive and negative sentiment lie at opposite ends, with neutral tweets forming a bridge connecting the two extremes. Both global and local scores assign higher centrality to this neutral region, reflecting its role as the manifold “middle”.

The dependence on t is relatively mild for this dataset. Global centrality peaks in the neutral band, while local centrality slightly sharpens dense subregions and decreases scores for more diffuse boundary points. Across all settings, the structure remains coherent, indicating a smooth sentiment trend.

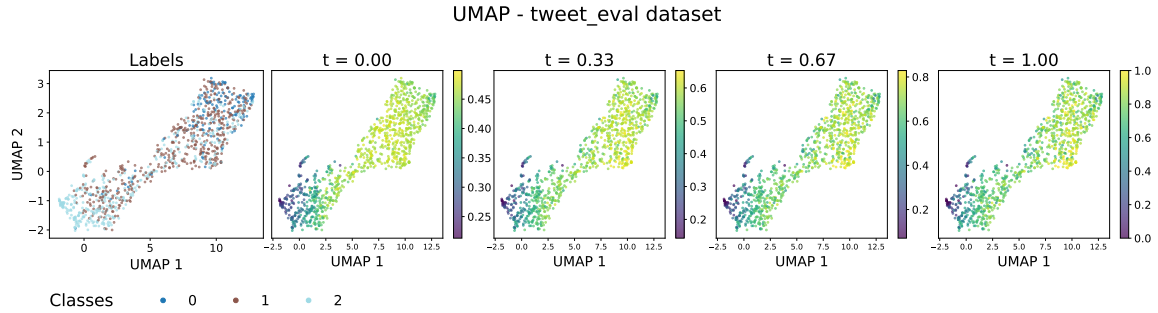


Figure 7: Homotopy centrality on TweetEval.

3.3 Outlier detection

We further assess the effectiveness of FUSE for outlier detection in low and moderately high-dimensional Euclidean data. We consider two benchmark datasets, Breastw and Ionosphere, drawn from the ADBench and ODDS libraries with standard anomaly labels inherited from the original classification tasks. We use the standardized, preprocessed versions provided by Bouman et al. (2024) in their public GitHub repository.¹ Following the distinction between global and local density anomalies as discussed in (Foorthuis, 2021; Bouman et al., 2024), Breastw ($n = 683$, $d = 9$) behaves as a global anomaly problem, since the anomalous classes are small but clinically distinct, and tend to occupy regions of globally low density relative to the main mass of normal samples. In contrast, Ionosphere ($n = 351$, $d = 33$) is a prototypical local anomaly problem, where anomalous points lie in regions whose density is low compared to nearby normal regions rather than forming a single, clearly separated peripheral cluster.

We compare three variants of our method, Global, Local, and the interpolated family FUSE, with four standard one-class baselines, including Isolation Forest (IF; Liu et al.

1. <https://github.com/RoelBouman/outlierdetection>.

2008), Kernel Density Estimation (KDE; Parzen 1962; Silverman 2018), Local Outlier Factor (LOF; Breunig et al. 2000), and One-Class SVM (OCSVM; Schölkopf et al. 2001). For FUSE, we consider a grid of homotopy parameters $t \in \{0.1, 0.2, \dots, 0.9\}$ and treat t as a hyperparameter. Hence, in Table 3, the single “FUSE” column reports the cross-validated choice of t . All four baselines use the `scikit-learn` (Pedregosa et al., 2011) implementations, and we tune hyperparameters for both the baselines and our three variants by cross-validation. Full grids and training details are given in Supplement S4.

Table 3: Outlier detection performance on Breastw and Ionosphere.

Dataset	Metric	Global	Local	FUSE	IF	LOF	OCSVM	KDE
Breastw	AUC-ROC	0.988	0.987	0.990	0.987	0.497	0.962	0.981
	AUC-PRC	0.976	0.961	0.979	0.971	0.353	0.908	0.948
Ionosphere	AUC-ROC	0.870	0.959	0.958	0.853	0.903	0.764	0.942
	AUC-PRC	0.875	0.950	0.950	0.810	0.859	0.773	0.938

Table 3 reports both AUC-ROC and AUC-PRC for Breastw and Ionosphere. On Breastw, where anomalies correspond to small but clinically distinct diagnostic classes and global shifts dominate, Global already performs very strongly: it attains AUC-ROC 0.988 and AUC-PRC 0.976, outperforming all classical baselines. IF and KDE are the strongest among the baselines, but still fall slightly short of Global in both metrics, while LOF collapses on this dataset. FUSE provides a modest further gain, achieving the best overall performance with AUC-ROC 0.990 and AUC-PRC 0.979, slightly improving over both Global and Local.

Ionosphere presents a different challenge, with substantial overlap between normal and anomalous samples and anomalies manifesting primarily as local neighborhood irregularities. Here Global lags behind density-based methods, with AUC-ROC 0.870 and AUC-PRC 0.875. In contrast, Local and FUSE variants perform markedly better. Local achieves AUC-ROC 0.959 and AUC-PRC 0.950, and FUSE attains essentially the same values, both clearly outperforming Global and the classical baselines. KDE and LOF are also strong on this dataset, but remain below Local and FUSE on both metrics.

Overall, these results illustrate that the three FUSE variants capture complementary aspects of abnormality. Global aligns well with datasets dominated by broad distributional shifts (Breastw), Local is more effective when anomalies are primarily local irregularities (Ionosphere), and FUSE interpolates between them to provide robust performance without prior knowledge of whether a given dataset is “global” or “local” in nature.

4 Conclusion and Discussion

We presented FUSE, a neural framework for estimating centrality that combines two complementary signals: a global ranking head capturing large-scale geometric structure, and

a local score-matching head capturing density-based typicality. A homotopy interpolation links these two regimes, yielding a continuum of centrality scores that trade off global robustness and local sensitivity. This unified design enables FUSE to operate across heterogeneous data types and to provide interpretable, scalable centrality estimates in high-dimensional and non-Euclidean settings.

From a practical standpoint, FUSE is best viewed as a lightweight module operating on fixed representations, with a simple trainable architecture. In our experiments we use a shared encoder consisting of two fully connected layers with GELU activations (Hendrycks, 2016) and width q , followed by linear heads for the global and local scores. Choosing $q \in \{32, 64, 128\}$ already yields strong performance across all of our benchmarks. For more complex data, practitioners can increase the width or depth of this encoder, or replace it with a domain-specific neural network, while keeping the FUSE heads and loss functions unchanged.

Future directions include exploring alternative similarity notions, extending the framework to more structured or multimodal data, and developing a more systematic understanding of how to adapt the noise parameter η for arbitrary data types. Overall, we hope FUSE provides a flexible foundation for incorporating depth and centrality ideas into modern neural models and for developing more interpretable, geometry-aware learning systems.

References

- Claudio Agostinelli and Mario Romanazzi. Local depth. *Journal of Statistical Planning and Inference*, 141(2):817–830, 2011.
- Francesco Barbieri, Jose Camacho-Collados, Leonardo Neves, and Luis Espinosa-Anke. Tweeteval: Unified benchmark and comparative evaluation for tweet classification. *arXiv preprint arXiv:2010.12421*, 2020.
- Mikhail Belkin, Partha Niyogi, and Vikas Sindhwani. Manifold regularization: A geometric framework for learning from labeled and unlabeled examples. *Journal of machine learning research*, 7(11), 2006.
- Liron Bergman and Yedid Hoshen. Classification-based anomaly detection for general data. In *International Conference on Learning Representations*, 2020.
- Kevin Beyer, Jonathan Goldstein, Raghu Ramakrishnan, and Uri Shaft. When is “nearest neighbor” meaningful? In *International conference on database theory*, pages 217–235. Springer, 1999.
- Hannah Blocher and Georg Schollmeyer. Union-free generic depth for non-standard data. *arXiv preprint arXiv:2412.14745*, 2024.

- Roel Bouman, Zaharah Bukhsh, and Tom Heskes. Unsupervised anomaly detection algorithms on real-world data: how many do we need? *Journal of Machine Learning Research*, 25(105):1–34, 2024.
- Ralph Allan Bradley and Milton E Terry. Rank analysis of incomplete block designs: I. the method of paired comparisons. *Biometrika*, 39(3/4):324–345, 1952.
- Markus M Breunig, Hans-Peter Kriegel, Raymond T Ng, and Jörg Sander. Lof: identifying density-based local outliers. In *Proceedings of the 2000 ACM SIGMOD international conference on Management of data*, pages 93–104, 2000.
- Ting Chen, Simon Kornblith, Mohammad Norouzi, and Geoffrey Hinton. A simple framework for contrastive learning of visual representations. In *International conference on machine learning*, pages 1597–1607. PmLR, 2020.
- Xiongtao Dai, Sara Lopez-Pintado, and Alzheimer’s Disease Neuroimaging Initiative. Tukey’s depth for object data. *Journal of the American Statistical Association*, 118(543):1760–1772, 2023.
- Hoang Anh Dau, Anthony Bagnall, Kaveh Kamgar, Chin-Chia Michael Yeh, Yan Zhu, Shaghayegh Gharghabi, Chotirat Ann Ratanamahatana, and Eamonn Keogh. The ucr time series archive. *IEEE/CAA Journal of Automatica Sinica*, 6(6):1293–1305, 2019.
- Jacob Devlin, Ming-Wei Chang, Kenton Lee, and Kristina Toutanova. Bert: Pre-training of deep bidirectional transformers for language understanding. In *Proceedings of the 2019 conference of the North American chapter of the association for computational linguistics: human language technologies, volume 1 (long and short papers)*, pages 4171–4186, 2019.
- Xiaowen Dong, Dorina Thanou, Pascal Frossard, and Pierre Vandergheynst. Learning laplacian matrix in smooth graph signal representations. *IEEE Transactions on Signal Processing*, 64(23):6160–6173, 2016.
- David L Donoho and Miriam Gasko. Breakdown properties of location estimates based on halfspace depth and projected outlyingness. *Annals of Statistics*, 20(4):1803–1827, 1992.
- Subhajit Dutta, Anil K Ghosh, and Probal Chaudhuri. Some intriguing properties of tukey’s half-space depth. *Bernoulli*, pages 1420–1434, 2011.
- Rainer Dyckerhoff and Pavlo Mozharovskyi. Exact computation of the halfspace depth. *Computational Statistics & Data Analysis*, 98:19–30, 2016.
- Rainer Dyckerhoff, Pavlo Mozharovskyi, and Stanislav Nagy. Approximate computation of projection depths. *Computational Statistics & Data Analysis*, 157:107166, 2021.
- Antonio Elías, Raúl Jiménez, Anna M Paganoni, and Laura M Sangalli. Integrated depths for partially observed functional data. *Journal of computational and graphical statistics*, 32(2):341–352, 2023.

- Charles Fefferman, Sanjoy Mitter, and Hariharan Narayanan. Testing the manifold hypothesis. *Journal of the American Mathematical Society*, 29(4):983–1049, 2016.
- Roman Feldbauer and Arthur Flexer. A comprehensive empirical comparison of hubness reduction in high-dimensional spaces. *Knowledge and Information Systems*, 59(1):137–166, 2019.
- Vít Fojtík, Petra Laketa, Pavlo Mozharovskyi, and Stanislav Nagy. On exact computation of tukey depth central regions. *Journal of Computational and Graphical Statistics*, 33(2): 699–713, 2024.
- Ralph Foorthuis. On the nature and types of anomalies: a review of deviations in data. *International journal of data science and analytics*, 12(4):297–331, 2021.
- Giacomo Francisci, Claudio Agostinelli, Alicia Nieto-Reyes, and Anand N Vidyashankar. Analytical and statistical properties of local depth functions motivated by clustering applications. *Electronic Journal of Statistics*, 17(1):688–722, 2023.
- Zengyou He, Xiaofei Xu, and Shengchun Deng. Discovering cluster-based local outliers. *Pattern recognition letters*, 24(9-10):1641–1650, 2003.
- D Hendrycks. Gaussian error linear units (gelus). *arXiv preprint arXiv:1606.08415*, 2016.
- Aapo Hyvärinen and Peter Dayan. Estimation of non-normalized statistical models by score matching. *Journal of Machine Learning Research*, 6(4), 2005.
- Maurice G Kendall. A new measure of rank correlation. *Biometrika*, 30(1/2):81–93, 1938.
- Alex Krizhevsky, Geoffrey Hinton, et al. Learning multiple layers of features from tiny images. 2009.
- Yann LeCun, Léon Bottou, Yoshua Bengio, and Patrick Haffner. Gradient-based learning applied to document recognition. *Proceedings of the IEEE*, 86(11):2278–2324, 2002.
- Yaron Lipman, Ricky TQ Chen, Haggai Ben-Hamu, Maximilian Nickel, and Matthew Le. Flow matching for generative modeling. In *International Conference on Learning Representations (ICLR)*, 2023.
- Fei Tony Liu, Kai Ming Ting, and Zhi-Hua Zhou. Isolation forest. In *2008 eighth ieee international conference on data mining*, pages 413–422. IEEE, 2008.
- Regina Y Liu. On a notion of data depth based on random simplices. *The Annals of Statistics*, pages 405–414, 1990.
- Carl H Lubba, Sarab S Sethi, Philip Knaute, Simon R Schultz, Ben D Fulcher, and Nick S Jones. catch22: Canonical time-series characteristics: Selected through highly comparative time-series analysis. *Data mining and knowledge discovery*, 33(6):1821–1852, 2019.

- P. C. Mahalanobis. On the generalised distance in statistics. *Proceedings of the National Institute of Sciences of India*, 2:49–55, 1936.
- Leland McInnes, John Healy, and James Melville. Umap: Uniform manifold approximation and projection for dimension reduction. *arXiv preprint arXiv:1802.03426*, 2018.
- Marina Meilă and Hanyu Zhang. Manifold learning: What, how, and why. *Annual Review of Statistics and Its Application*, 11(1):393–417, 2024.
- Emanuel Parzen. On estimation of a probability density function and mode. *The annals of mathematical statistics*, 33(3):1065–1076, 1962.
- Fabian Pedregosa, Gaël Varoquaux, Alexandre Gramfort, Vincent Michel, Bertrand Thirion, Olivier Grisel, Mathieu Blondel, Peter Prettenhofer, Ron Weiss, Vincent Dubourg, et al. Scikit-learn: Machine learning in python. *the Journal of machine Learning research*, 12:2825–2830, 2011.
- Oleksii Pokotylo and Karl Mosler. Classification with the pot–pot plot. *Statistical Papers*, 60(3):903–931, 2019.
- Alec Radford, Jong Wook Kim, Chris Hallacy, Aditya Ramesh, Gabriel Goh, Sandhini Agarwal, Girish Sastry, Amanda Askell, Pamela Mishkin, Jack Clark, et al. Learning transferable visual models from natural language supervision. In *International conference on machine learning*, pages 8748–8763. PmLR, 2021.
- Milos Radovanovic, Alexandros Nanopoulos, and Mirjana Ivanovic. Hubs in space: Popular nearest neighbors in high-dimensional data. *Journal of Machine Learning Research*, 11 (sept):2487–2531, 2010.
- Alex Rodriguez and Alessandro Laio. Clustering by fast search and find of density peaks. *science*, 344(6191):1492–1496, 2014.
- Lukas Ruff, Robert Vandermeulen, Nico Goernitz, Lucas Deecke, Shoaib Ahmed Siddiqui, Alexander Binder, Emmanuel Müller, and Marius Kloft. Deep one-class classification. In *International conference on machine learning*, pages 4393–4402. PMLR, 2018.
- Victor Sanh, Lysandre Debut, Julien Chaumond, and Thomas Wolf. Distilbert, a distilled version of bert: smaller, faster, cheaper and lighter. *arXiv preprint arXiv:1910.01108*, 2019.
- Bernhard Schölkopf, John C Platt, John Shawe-Taylor, Alex J Smola, and Robert C Williamson. Estimating the support of a high-dimensional distribution. *Neural computation*, 13(7):1443–1471, 2001.
- Robert Serfling. A depth function and a scale curve based on spatial quantiles. In *Statistical data analysis based on the L1-norm and related methods*, pages 25–38. Springer, 2002.

- Bernard W Silverman. *Density estimation for statistics and data analysis*. Routledge, 2018.
- Richard Socher, Alex Perelygin, Jean Wu, Jason Chuang, Christopher D Manning, Andrew Y Ng, and Christopher Potts. Recursive deep models for semantic compositionality over a sentiment treebank. In *Proceedings of the 2013 conference on empirical methods in natural language processing*, pages 1631–1642, 2013.
- Yang Song, Jascha Sohl-Dickstein, Diederik Kingma, Abhishek Kumar, Stefano Ermon, and Ben Poole. Score-based generative modeling through stochastic differential equations. *International Conference on Learning Representations (ICLR)*, 2021.
- C Spearman. The proof and measurement of association between two things. *American Journal of Psychology*, 15:72–101, 1904.
- Swabha Swayamdipta, Roy Schwartz, Nicholas Lourie, Yizhong Wang, Hannaneh Hajishirzi, Noah A Smith, and Yejin Choi. Dataset cartography: Mapping and diagnosing datasets with training dynamics. *arXiv preprint arXiv:2009.10795*, 2020.
- John W Tukey. Mathematics and the picturing of data. In *Proceedings of the international congress of mathematicians*, volume 2, pages 523–531. Vancouver, 1975.
- Yehuda Vardi and Cun-Hui Zhang. The multivariate l 1-median and associated data depth. *Proceedings of the National Academy of Sciences*, 97(4):1423–1426, 2000.
- Pascal Vincent. A connection between score matching and denoising autoencoders. *Neural computation*, 23(7):1661–1674, 2011.
- Hyemin Yeon, Xiongtao Dai, and Sara Lopez-Pintado. Regularized halfspace depth for functional data. *Journal of the Royal Statistical Society Series B: Statistical Methodology*, page qkaf030, 2025.
- Yijun Zuo. Projection-based depth functions and associated medians. *The Annals of Statistics*, 31(5):1460–1490, 2003.
- Yijun Zuo and Robert Serfling. General notions of statistical depth function. *Annals of statistics*, pages 461–482, 2000.

Supplementary Material for “A Trainable Centrality Framework for Modern Data”

Appendix S1. Neural architecture for FUSE

For all experiments, the trainable part of FUSE follows a common pipeline. Starting from the fixed representations $Z_i = \psi(X_i)$, we apply a shared encoder $e_{\theta_e} : \mathbb{R}^p \rightarrow \mathbb{R}^q$ implemented as two fully connected layers with GELU (Hendrycks, 2016) activations, followed by a linear projection to a q -dimensional feature. This shared feature is then passed to two scalar linear heads: the global ranking head g_θ and the local DSM head l_θ , as described in Section 2. In all our experiments, the hidden width of the encoder and the projection dimension q are taken to be the same (e.g., $q \in \{32, 64, 128\}$ depending on the setting).

The only architectural difference across experimental settings is this hidden width, which is chosen to reflect the complexity and dimensionality of the inputs:

- **Synthetic data (Section 3.1).** The shared encoder uses width (32, 32) for the two hidden layers, followed by a 32-dimensional linear projection (so $q = 32$). These low-dimensional toy examples mainly serve to validate qualitative depth-like behavior, so a small network suffices.
- **Real-data visualizations (Section 3.2).** For image, time series, and text experiments based on pretrained embeddings, we use width (64, 64) and a 64-dimensional projection (so $q = 64$). The representations are moderately high-dimensional but already informative, so we use a slightly larger encoder while avoiding overparameterization.
- **Outlier detection (Section 3.3).** For the ODDS datasets, we operate directly on raw feature vectors. To capture more complex structure in these inputs, we use two hidden layers of size (128, 128) and a 128-dimensional projection (so $q = 128$) in the shared encoder.

In all experiments, the number of anchor points per global pair is fixed at 64, and each data point is perturbed 8 times per epoch for the DSM objective. All models are trained for 30 epochs using the Adam optimizer (learning rate 10^{-3} , weight decay 0.0, batch size 128). GELU activations are used between hidden layers, no dropout is applied, and the heads g_θ and l_θ are implemented as single-layer linear maps on top of the shared encoder output.

Appendix S2. Different sampling strategy investigation

We evaluate four global sampling schemes for constructing triplets (S_0, S_1, S_2) used to train the global head. Throughout this section, let the training sample be $\{X_i\}_{i=1}^n$. Each scheme, denoted Schemes 1–4, specifies how anchors and candidate pairs are drawn from $\{X_i\}_{i=1}^n$ in order to estimate the pairwise ranking probabilities $\hat{\pi}(X_i, X_j)$ defined in Section 2.1.1.

Scheme 1 (default). We randomly partition the sample into three disjoint subsets of (approximately) equal size,

$$S_0 \cup S_1 \cup S_2 = \{X_i\}_{i=1}^n, \quad S_a \cap S_b = \emptyset \text{ for } a \neq b \in \{0, 1, 2\}.$$

We then form $\lfloor n/3 \rfloor$ candidate pairs (X_i, X_j) with $X_i \in S_1$ and $X_j \in S_2$ by matching elements by index, and, for each pair, sample a small number (64 in the experiments) of anchors from S_0 to estimate $\hat{\pi}(X_i, X_j)$. This scheme provides a good balance between efficiency and accuracy and is used as the default configuration in all main experiments.

Scheme 2. We use the same partitioning as in Scheme 1, but instead of index-wise matching, we form all possible pairs between S_1 and S_2 , i.e., the Cartesian product $S_1 \times S_2$, which yields $O(n^2)$ candidate pairs. Anchors are still subsampled from S_0 for each pair.

Scheme 3. This scheme is identical to Scheme 2 in how candidate pairs are formed, but all anchors in S_0 are used when estimating $\hat{\pi}(X_i, X_j)$ (no subsampling). It therefore corresponds to an exhaustive anchor-selection strategy.

Scheme 4. The most exhaustive variant sets

$$S_0 = S_1 = S_2 = \{X_i\}_{i=1}^n,$$

so that anchors and candidates can be any points in the sample. This produces $O(n^3)$ triplets $(X_{i_0}, X_{i_1}, X_{i_2})$ and is primarily of conceptual interest due to its high computational cost.

Empirical comparison. We compare all four schemes under the same experimental settings as in the main paper, covering both synthetic data and outlier detection tasks. All models use identical hyperparameters. Schemes 1 and 2 sample 64 anchors per candidate pair, while Schemes 3 and 4 use all available anchors.

Figures S1–S4 and Tables S1–S3 report the synthetic results. The design follows Section 3.1, but with 1000 (rather than 5000) two-dimensional samples in each setting to reduce computational cost. Figures S1–S4 visualize the homotopy centrality contours across different distributions and sampling schemes, while Tables S1–S3 summarize Spearman’s and Kendall’s rank correlations on the test set, as well as model training time and average inference time per sample. Tables S4–S5 report the detailed results for the outlier detection experiments in Section 3.3. The network architecture follows Supplement S1, and here we use a fixed configuration with two hidden layers of size (128, 128). In contrast to Section 3.3, where hyperparameters are tuned by cross-validation, all parameters are kept fixed in this supplement to reduce computational cost. These tables therefore illustrate the behavior of FUSE under a simple default architecture, while the main results in Section 3.3 correspond to tuned models.

Across all datasets, the four schemes yield very similar rank correlations and detection accuracy. However, Scheme 1 achieves this performance with substantially lower compu-

tational and memory cost. We therefore adopt Scheme 1 as the default global sampling configuration in all experiments reported in the paper.

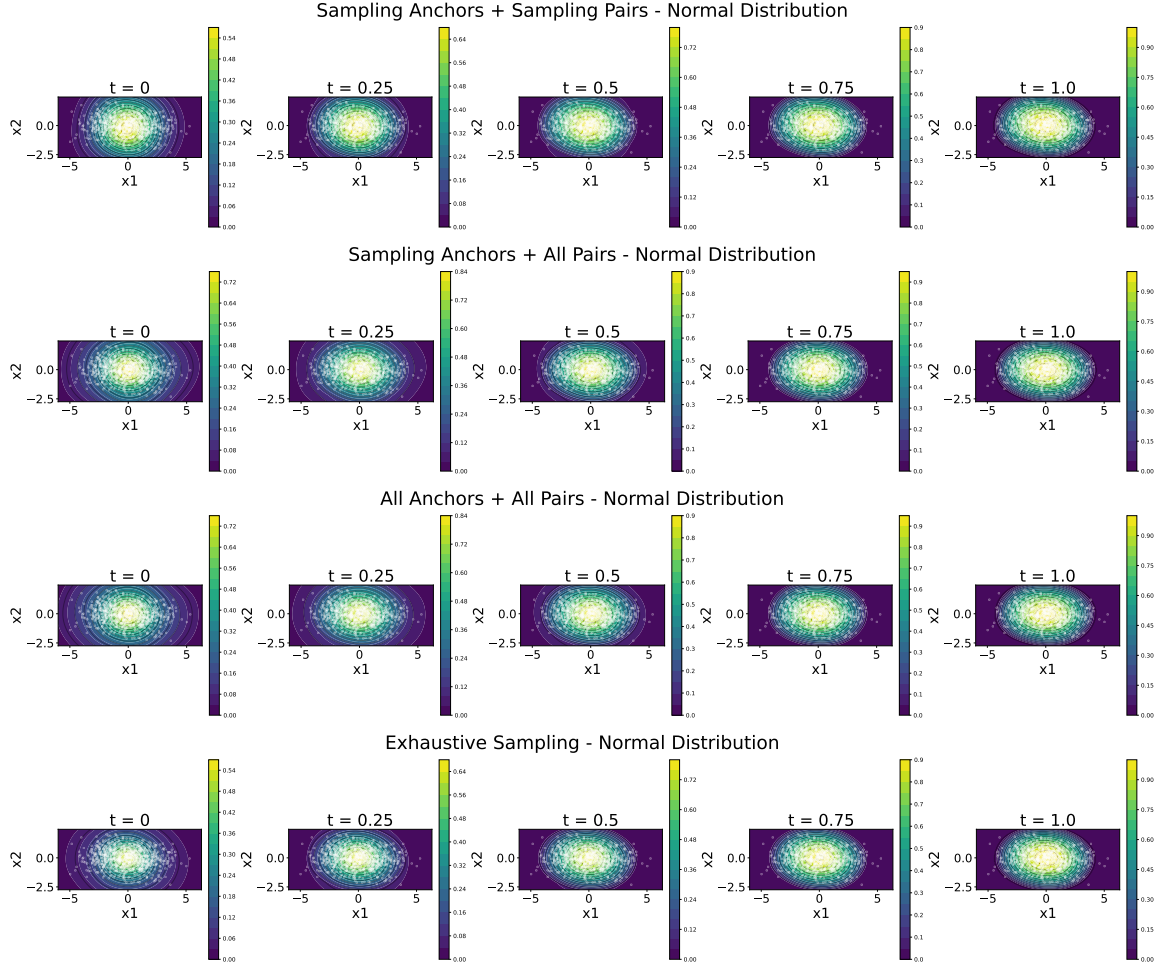


Figure S1: Homotopy centrality contours on Normal distribution.

Appendix S3. Depth function implementations

For benchmarking, we re-implemented several classical depth functions in Python, following the formulations in the `data-depth` package.² Let the reference sample be $\{X_i\}_{i=1}^n \subset \mathbb{R}^d$, and let $X_{1:n} \in \mathbb{R}^{n \times d}$ denote the corresponding data matrix with rows X_i^\top . Each depth function takes $X_{1:n}$ as reference and evaluates a depth value for a query point $x \in \mathbb{R}^d$.

2. <https://github.com/data-depth/library>

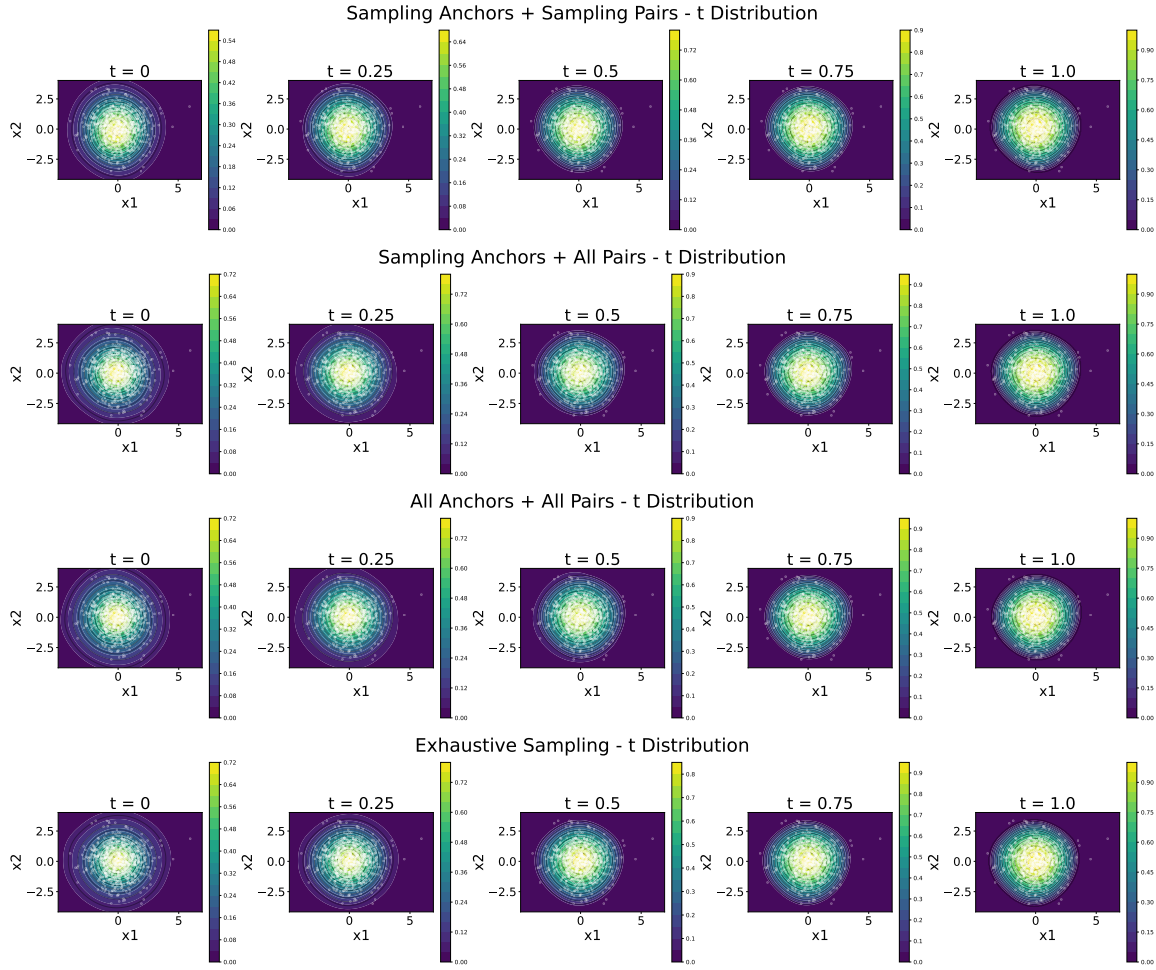

Figure S2: Homotopy centrality contours on Student- t_{10} distribution.

Table S1: Spearman's ρ , Kendall's τ , training time, and average inference time per sample on the Normal distribution.

Algorithm	Spearman	Kendall	Train Time (s)	Infer Time (ms)
Scheme 1 (Global)	0.9887	0.9095	4.81	0.369
Scheme 1 (Local)	0.9778	0.8807	4.81	0.369
Scheme 2 (Global)	0.9899	0.9168	137.08	0.379
Scheme 2 (Local)	0.9758	0.8773	137.08	0.379
Scheme 3 (Global)	0.9909	0.9216	101.68	0.478
Scheme 3 (Local)	0.9799	0.8895	101.68	0.478
Scheme 4 (Global)	0.9928	0.9353	609.46	0.420
Scheme 4 (Local)	0.9732	0.8712	609.46	0.420

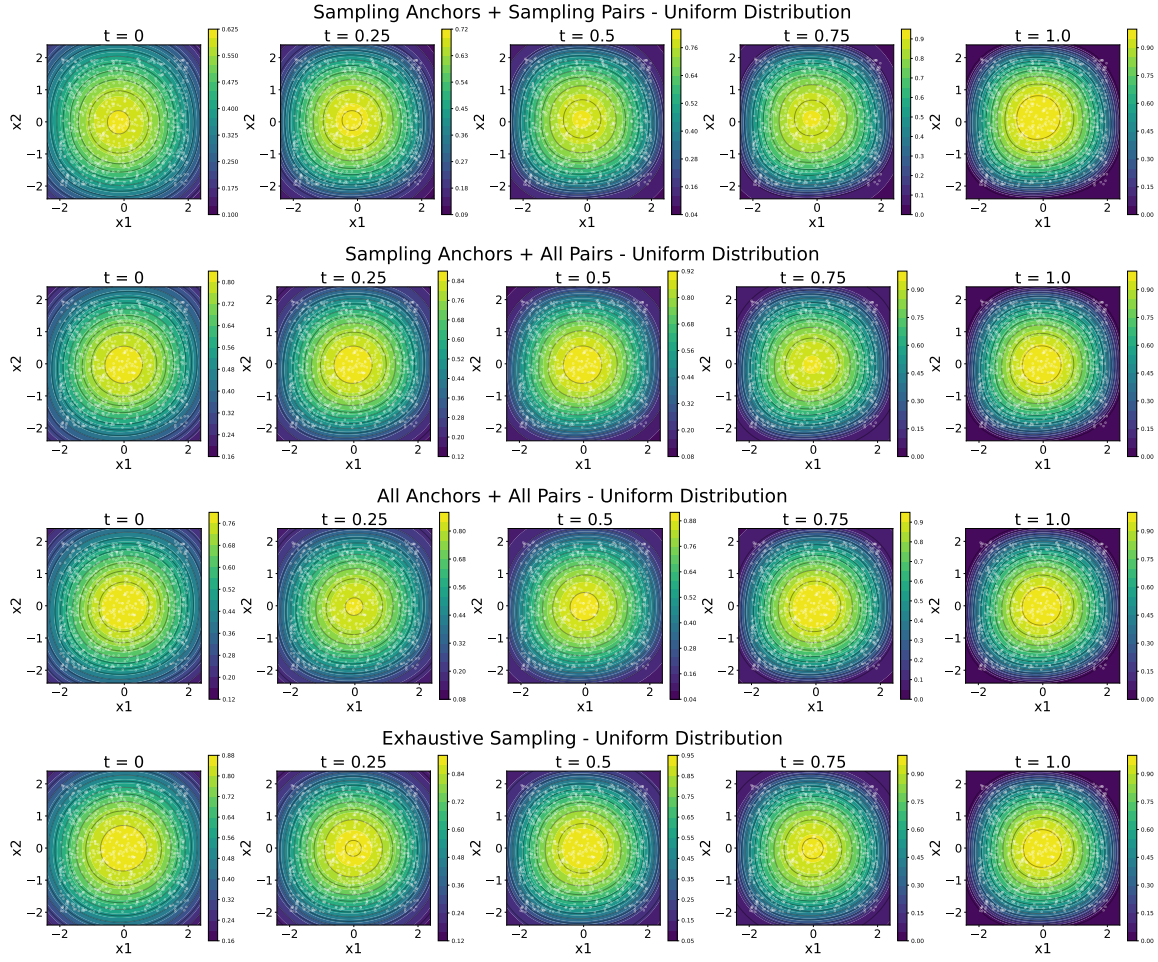


Figure S3: Homotopy centrality contours on Uniform distribution.

Table S2: Spearman's ρ , Kendall's τ , training time, and average inference time per sample on the Student- t_{10} distribution.

Algorithm	Spearman	Kendall	Train Time (s)	Infer Time (ms)
Scheme 1 (Global)	0.9953	0.9421	4.78	0.349
Scheme 1 (Local)	0.9986	0.9684	4.78	0.349
Scheme 2 (Global)	0.9941	0.9343	158.86	0.476
Scheme 2 (Local)	0.9972	0.9546	158.86	0.476
Scheme 3 (Global)	0.9943	0.9355	127.09	0.485
Scheme 3 (Local)	0.9989	0.9720	127.09	0.485
Scheme 4 (Global)	0.9990	0.9740	569.43	0.607
Scheme 4 (Local)	0.9984	0.9670	569.43	0.607

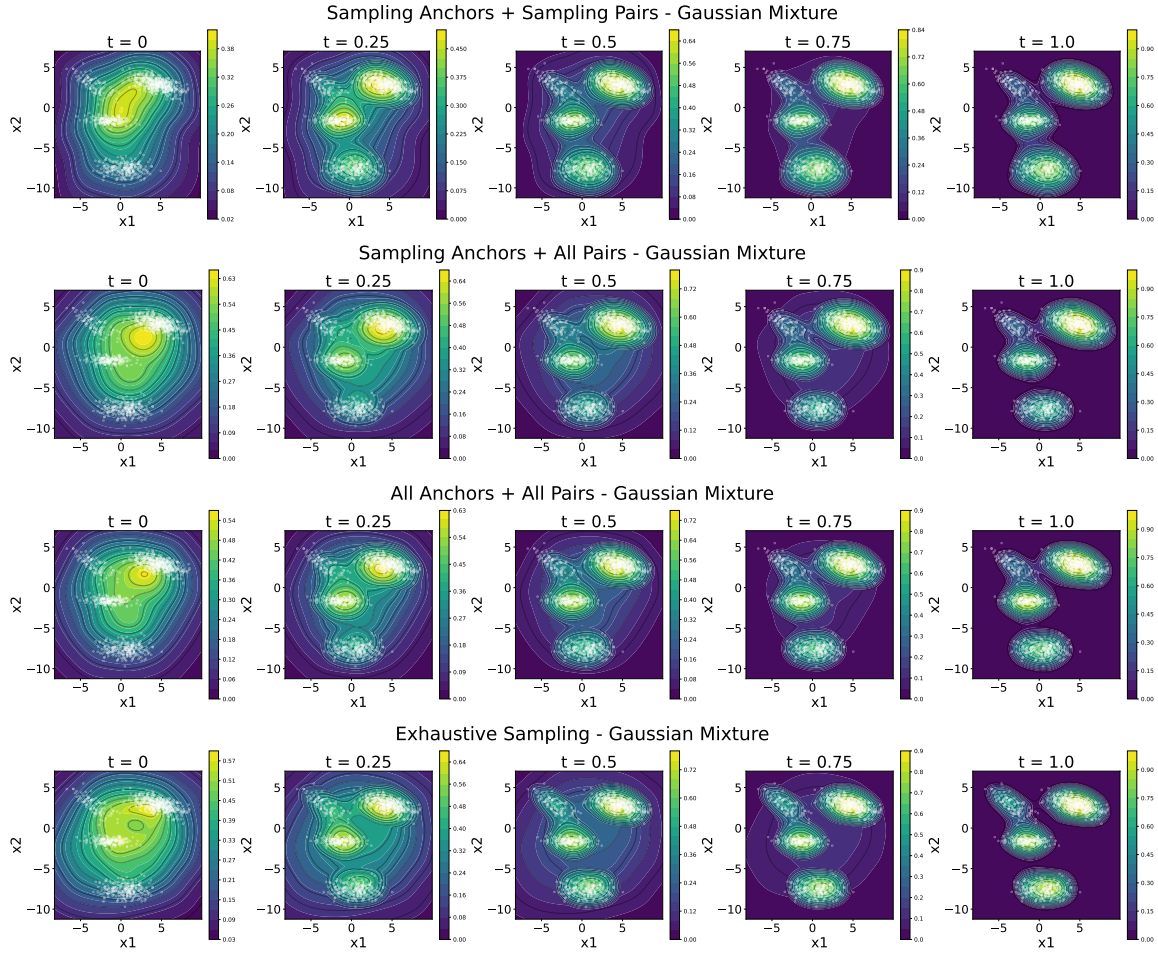


Figure S4: Homotopy centrality contours on Gaussian mixture.

Table S3: Spearman's ρ , Kendall's τ , training time, and average inference time per sample on the Uniform distribution.

Algorithm	Spearman	Kendall	Train Time (s)	Infer Time (ms)
Scheme 1 (Global)	0.9957	0.9460	4.86	0.506
Scheme 1 (Local)	0.9877	0.9032	4.86	0.506
Scheme 2 (Global)	0.9926	0.9281	137.73	0.581
Scheme 2 (Local)	0.9718	0.8523	137.73	0.581
Scheme 3 (Global)	0.9968	0.9524	100.51	0.543
Scheme 3 (Local)	0.9891	0.9115	100.51	0.543
Scheme 4 (Global)	0.9922	0.9272	589.98	0.468
Scheme 4 (Local)	0.9851	0.8994	589.98	0.468

Table S4: Test AUC-ROC, AUC-PRC, training time, and average inference time per sample for the Breastw dataset.

Model	AUC-ROC	AUC-PRC	Train Time (s)	Infer Time (ms)
Scheme 1 (Global)	0.950	0.912	4.227	1.276
Scheme 1 (Local)	0.983	0.953	4.227	1.276
Scheme 2 (Global)	0.945	0.906	18.056	1.132
Scheme 2 (Local)	0.983	0.955	18.056	1.132
Scheme 3 (Global)	0.948	0.902	14.358	1.590
Scheme 3 (Local)	0.984	0.955	14.358	1.590
Scheme 4 (Global)	0.954	0.931	92.718	1.336
Scheme 4 (Local)	0.985	0.955	92.718	1.336

Table S5: Test AUC-ROC, AUC-PRC, training time, and average inference time per sample for Ionosphere dataset.

Model	AUC-ROC	AUC-PRC	Train Time (s)	Infer Time (ms)
Scheme 1 (Global)	0.758	0.748	0.961	0.653
Scheme 1 (Local)	0.891	0.854	0.961	0.653
Scheme 2 (Global)	0.779	0.744	3.873	0.535
Scheme 2 (Local)	0.865	0.818	3.873	0.535
Scheme 3 (Global)	0.742	0.714	3.477	0.767
Scheme 3 (Local)	0.862	0.818	3.477	0.767
Scheme 4 (Global)	0.757	0.719	19.312	0.937
Scheme 4 (Local)	0.859	0.806	19.312	0.937

Mahalanobis depth. (Mahalanobis, 1936) Let the sample mean and the sample variance be

$$\bar{X} = \frac{1}{n} \sum_{i=1}^n X_i, \quad \hat{\Sigma} = \frac{1}{n-1} \sum_{i=1}^n (X_i - \bar{X})(X_i - \bar{X})^\top.$$

For numerical stability, we add a small ridge εI_d with $\varepsilon = 10^{-9}$. The regularized Mahalanobis depth is

$$D_{\text{mah}}(x \mid X_{1:n}) = \frac{1}{1 + (x - \bar{X})^\top (\hat{\Sigma} + \varepsilon I_d)^{-1} (x - \bar{X})}.$$

Instead of explicitly inverting $\hat{\Sigma}$, we compute a Cholesky factorization $LL^\top = \hat{\Sigma} + \varepsilon I_d$ and evaluate the quadratic form as $\|L^{-1}(x - \bar{X})\|_2^2$ for efficiency.

Spatial depth. (Serfling, 2002) Define the spatial sign function $s(v)$ by

$$s(v) = \begin{cases} v/\|v\|_2, & v \neq 0, \\ 0, & v = 0. \end{cases}$$

For affine invariance, we whiten the data using the moment covariance. Let B satisfy $BB^\top = (\hat{\Sigma} + \varepsilon I_d)^{-1}$ with $\varepsilon = 10^{-12}$, and define $\check{X}_i = B(X_i - \bar{X})$ and $\check{x} = B(x - \bar{X})$. The spatial depth is then

$$D_{\text{spat}}(x \mid X_{1:n}) = 1 - \left\| \frac{1}{n} \sum_{i=1}^n s(\check{x} - \check{X}_i) \right\|_2.$$

Potential depth. (Pokotylo and Mosler, 2019) We follow the kernel-based formulation of Pokotylo and Mosler (2019), but omit whitening for improved numerical stability in high dimensions. Given a query point x and reference sample $\{X_i\}_{i=1}^n$, define distances $r_i = \|x - X_i\|_2$. The bandwidth parameter $\beta > 0$ is chosen by Scott’s rule $\beta = n^{-2/(d+4)}$, and is clamped below by a small $\varepsilon = 10^{-12}$ for stability. The potential depth is the average of a radial kernel:

$$D_{\text{pot}}(x \mid X_{1:n}) = \frac{1}{n} \sum_{i=1}^n K_\beta(r_i), \quad K_\beta(r) = \exp(-\beta r^2) \text{ (Gaussian kernel)}.$$

Projection depth. (Dyckerhoff et al., 2021) We approximate the Stahel–Donoho outlyingness by sampling K random unit directions $u_k \in \mathbb{S}^{d-1}$ and computing

$$D_{\text{proj}}(x \mid X_{1:n}) = \frac{1}{1 + \max_{k \leq K} \frac{|\langle x, u_k \rangle - \text{med}(\langle X, u_k \rangle)|}{\text{MAD}(\langle X_{1:n}, u_k \rangle)}}.$$

Here $\langle X_{1:n}, u_k \rangle$ denotes the vector $(\langle X_1, u_k \rangle, \dots, \langle X_n, u_k \rangle)^\top$, and med and MAD are the univariate median and median absolute deviation.

Tukey depth. (Tukey, 1975) We approximate the Tukey depth using its projection-min characterization. Sampling K random directions $u_k \in \mathbb{S}^{d-1}$, we project X and x onto each u_k , compute the univariate Tukey depth in the projected space, and take the minimum:

$$D_{\text{half}}(x \mid X_{1:n}) = \min_{k \leq K} D_{\text{tukey}}(\langle x, u_k \rangle \mid \langle X_{1:n}, u_k \rangle).$$

Direction sampling for projection-based methods. Both projection depth and half-space depth rely on random directions to approximate directional extrema. To balance runtime and accuracy, we use

$$K = \text{clip}(n \times 2^{d-1}, 100, 50,000), \quad \text{clip}(x, a, b) = \min\{\max\{x, a\}, b\}.$$

This rule scales the direction budget with dimensionality while keeping computation tractable: at least 100 directions are used in low dimensions, and a maximum of 50,000 directions caps the cost in higher dimensions. This setting achieves a good trade-off between approximation accuracy and computational efficiency across all datasets.

Appendix S4. Outlier detection experiment settings

Cross-validation and model selection. We use a simple 5-fold scheme without nested inner loops. For outer fold $k \in \{0, 1, 2, 3, 4\}$, fold k serves as the test set, fold $(k+1) \bmod 5$ as the validation set, and the remaining three folds as the training set. For each method and fold, hyperparameters are selected on the validation set by maximizing AUC-PRC (ties broken by AUC-ROC), after which the model is refit on the corresponding training folds and evaluated on the held-out test fold. Final numbers are the mean over the five test folds.

Metrics. We evaluate performance using area under the precision–recall curve (AUC-PRC) and area under the receiver-operating characteristic curve (AUC-ROC). Because anomalies are rare, AUC-PRC is our primary metric, and AUC-ROC is reported for completeness. For models whose raw outputs represent inlier scores (e.g., KDE log-density, IF/LOF decision scores), we negate the scores so that larger values consistently indicate stronger outlierness before computing the AUC metrics.

Hyperparameter grids. We use standard `scikit-learn` implementations with the hyperparameter grids listed below. Unless otherwise specified, all remaining parameters are kept at their `scikit-learn` default values.

- **IF** (`sklearn.ensemble.IsolationForest`): $n_{\text{estimators}} \in \{100, 200, 400\}$; $max_features \in \{1.0, 0.75, 0.5\}$; $max_samples = \text{"auto"}$; $bootstrap = \text{False}$.
- **LOF** (`sklearn.neighbors.LocalOutlierFactor`): $n_{\text{neighbors}} \in \{10, 20, 35, 50\}$; Minkowski order $p \in \{1, 2\}$ (L_1 or L_2); $leaf_size = 30$ (fixed); $novelty = \text{True}$.
- **OCSVM** (`sklearn.svm.OneClassSVM`): $\gamma \in \{\text{"scale"}, \text{"auto"}, 10^{-3}, 10^{-2}, 10^{-1}\}$; $\nu \in \{0.01, 0.05, 0.1, 0.2\}$; $max_iter = 10^5$.
- **KDE** (`sklearn.neighbors.KernelDensity`): $kernel \in \{\text{"gaussian"}, \text{"epanechnikov"}\}$; $bandwidth \in \{0.1, 0.2, 0.5, 1.0, 2.0\}$; $metric = \text{"euclidean"}$.
- **FUSE**: We use the architecture from Supplement S1 with shared-encoder width (128, 128). Distance metric $\in \{1, 2\}$ (L_1 or L_2); DSM noise scale $\eta \in \{0.1, 0.2, 0.5, 1.0, 2.0\}$; interpolation parameter $t \in \{0.1, 0.2, \dots, 0.9\}$; number of anchors = 64; DSM resamples per epoch = 8; batch size = 128; epochs = 30; learning rate = 10^{-3} . The endpoints $t=0$ and $t=1$ correspond to the Global and Local variants, respectively, and are reported separately.